

A Nanostructured Phenazine-Based Conjugated Microporous Polymer Hybrid Anode Boosts Power and Practicability of Organic-Manganese Hydronium-Ion Batteries

Rebecca Grieco,^[a] Alba Fombona-Pascual,^[a] Nagaraj Patil,*^[a] Diego Alvan,^[a] Marta Liras,^[b] and Rebeca Marcilla*^[a]

Organic-manganese hydronium-ion batteries are gaining attention for their safety, sustainability, and high rate capabilities. However, their electrochemical performance faces challenges due to organic active-materials' inferior properties, including low conductivity and solubility, and limited content (<60 wt%) and loading (<2 mg cm⁻²) in the anode. To address this, we developed a high-performance battery using a phenazine-based conjugated microporous polymer hybrid anode (IEP-27-SR), utilizing hydronium-ion coordination/un-coordination chemistry. The IEP-27-SR anode features enhanced structural characteristics, such as a high BET specific surface area, mixed micro-/mesoporosity, nanostructurization, and hybridization, enabling rapid hydronium-ion mobility. The resulting IEP-27-SR//MnO₂@GF full-cell demonstrates high capacity (101 mAh g⁻¹

at 2 C), excellent rate performance (41 mAh g⁻¹ at 100 C), ultrafast-charging capability (80% charged in 18 seconds), and impressive cycling stability with 83% capacity retention over 20400 cycles at 30 C with a regular polymer mass loading of 2 mg cm⁻², despite its high content (80 wt%) in the anode. Moreover, it shows operability at low temperatures (63 mAh g⁻¹ at -40 °C). Most importantly, the full-cell with a high-mass-loading polymer anode (30 mg cm⁻²) achieves practically relevant areal capacity (3.4 mAh cm⁻² at 4 mA cm⁻²) and sustains 2 mAh cm⁻² under an extremely high areal current (50 mA cm⁻²). This breakthrough highlights the progress of organic hydronium-ion batteries, representing progress toward practical, sustainable energy storage solutions.

Introduction

In recent years, Li-ion batteries (LIBs) have become the energy storage technology of choice for electric vehicles and portable electronics.^[1] Although their lightweight, high overall energy density and reasonable cycle life are appealing for mobile applications, their exploitation in large-scale stationary energy storage systems, for example, grid-scale energy storage, is still limited by the high costs involved, operational lifespan, and safety considerations.^[2] In this regard, aqueous rechargeable batteries (ARBs) have been projected as promising alternatives to traditional LIBs. These batteries provide notable benefits in terms of safety and cost effectiveness, due to the inherent characteristics of water-based electrolytes, which are non-

volatile, non-toxic and non-flammable.^[3] Additionally, ARBs offer the advantage of rapid charging and the ability to deliver high power densities due to the excellent ionic conductivity of aqueous electrolytes.^[3,4] To date, conventional aqueous batteries have utilized various types of charge carriers, which can be classified as either metallic, such as Al³⁺, Zn²⁺ and Mn²⁺ or non-metallic, such as H⁺, NH₄⁺, Cl⁻ and F⁻.^[5] Among them, proton (H⁺) stands out as a compelling contender within the category of non-metallic charge carriers due to its accelerated kinetics attributed to its minimal ionic mass, smallest radius,^[5-7] and rapid ionic conduction due to the genuine Grotthuss mechanism.^[3,8] However, due to the considerable energy required for the dehydration of H₃O⁺ (11.66 eV), the charge carriers present in the acidic solution are hydronium ions (H₃O⁺) instead of H⁺.^[9,10] Consequently, the higher ionic radius of H₃O⁺ (0.1 nm) requires the use of appropriate host electrode materials that can effectively accommodate hydronium ions.^[3]

Among the different types of hydronium ion batteries, those employing manganese (Mn)-based cathodes have garnered significant research and industry interest^[11-13] due to their low cost, environmental friendliness, high theoretical capacity, and energy density.^[14,15] The high electrochemical performance of these Mn-based batteries (abbreviated as MnBs) relies on the reversible storage mechanism recently discovered by Cui and co-workers, involving Mn²⁺/MnO₂ deposition/stripping on the cathode side.^[11] Subsequent efforts have been directed to identify a proper anode material that can work under acidic conditions and store hydronium ions without compromising its

[a] R. Grieco, A. Fombona-Pascual, N. Patil, D. Alvan, R. Marcilla
Electrochemical Processes Unit, IMDEA Energy Institute, Avda. Ramón de la Sagra 3, 28935 Móstoles, Spain
E-mail: nagaraj.patil@imdea.org
rebeca.marcilla@imdea.org

[b] M. Liras
Photoactivated Processes Unit, IMDEA Energy Institute, Avda. Ramón de la Sagra 3, 28935 Móstoles, Spain
Supporting information for this article is available on the WWW under
<https://doi.org/10.1002/batt.202400346>

© 2024 The Authors. *Batteries & Supercaps* published by Wiley-VCH GmbH. This is an open access article under the terms of the Creative Commons Attribution Non-Commercial NoDerivs License, which permits use and distribution in any medium, provided the original work is properly cited, the use is non-commercial and no modifications or adaptations are made.

structural stability. Although various battery configurations such as Pb-MnO₂,^[10] Cu-MnO₂,^[16] Bi-MnO₂,^[12] and Zn-MnO₂,^[17] have been explored, these batteries face significant drawbacks, including passivation, corrosion, and formation of dendrites in the anode side thus, compromising the cycling stability and safety of these batteries. Although other inorganic anodes such as MoO₃,^[18] and Mxene,^[19] have lately improved the cyclability of MnBs to some extent, they still lack high performance and mostly transmit unsustainable burdens.

Recently, organic electrode materials (OEMs)^[20] composed of light, readily available, and cost-effective elements such as carbon (C), oxygen (O), and nitrogen (N), have gained popularity as cost-effective and sustainable alternative anodes for MnBs.^[21–25] This is attributed to their distinctive ion coordination mechanism capable of enduring structural transformations while interacting with large charge carriers.^[26] Furthermore, OEMs do not encounter common issues observed in traditional anodes, such as dendrite formation (in metals) and corrosion (in metals and inorganic compounds), particularly under acidic conditions. Due to those advantages of OEMs, various MnBs bearing organic anodes, including small molecules,^[22,27] linear polymers,^[28,29] and conjugated porous polymers^[30] have been reported in recent years. In most examples, the redox-active functionalities were carbonyl-based moieties like quinones^[28,31] and anhydrides.^[22,27,32] However, recent studies have unveiled the promising electrochemical characteristics of alternative structures, such as nitrogen-containing organic compounds with C=N as active sites.^[33] These C=N-based organic materials have demonstrated the ability to store hydronium ions in various battery configurations, expanding their potential applications.^[24,34–36]

Despite the advantages of organic MnBs, their application is still limited by several factors: first of all, the low electrical conductivity of OEMs, which compels them to use high amounts of carbon additives in the electrode preparation (typically between 30 and 60 wt.%), then the limited cycle stability, mostly due to solubility issues faced by small molecules and some linear polymers, and, finally, the low active-material mass loading, which ensures a high capacity utilisation, but at the expense of areal capacity, cost and practicability. In fact, it is now widely recognised in the field of battery material design that electrodes must possess a significant content of active material (> 70 wt%) and exhibit a sufficiently high areal capacity (> 3 mAh cm⁻²) to effectively reduce the overall cost of the battery.^[37] In this scenario, incorporating redox functionalities into a cross-linked porous polymer framework has emerged as an intriguing strategy. This not only addresses solubility concerns and enhances kinetics and material utilization,^[35,38–41] but also facilitates efficient ion mobility by creating a shorter diffusion path. The porous structure minimizes charge transport limitations and guarantees high capacity utilisation and rate capability even under challenging conditions such as high mass loading electrodes (60 mg cm⁻²) or elevated polymer content (80 wt%) within the electrode.^[37]

Unfortunately, most of the reported organic MnBs have scarcely met these targets, therefore they are not able to fully

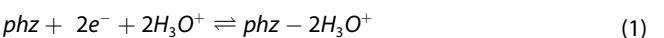
exploit the cost and sustainability advantages of OEMs for the development of practical batteries. Therefore, despite some recent promising developments,^[29] there is still a lack of high-performance anodes that can simultaneously show good rate capability and long cycling, especially under practical mass loading conditions.

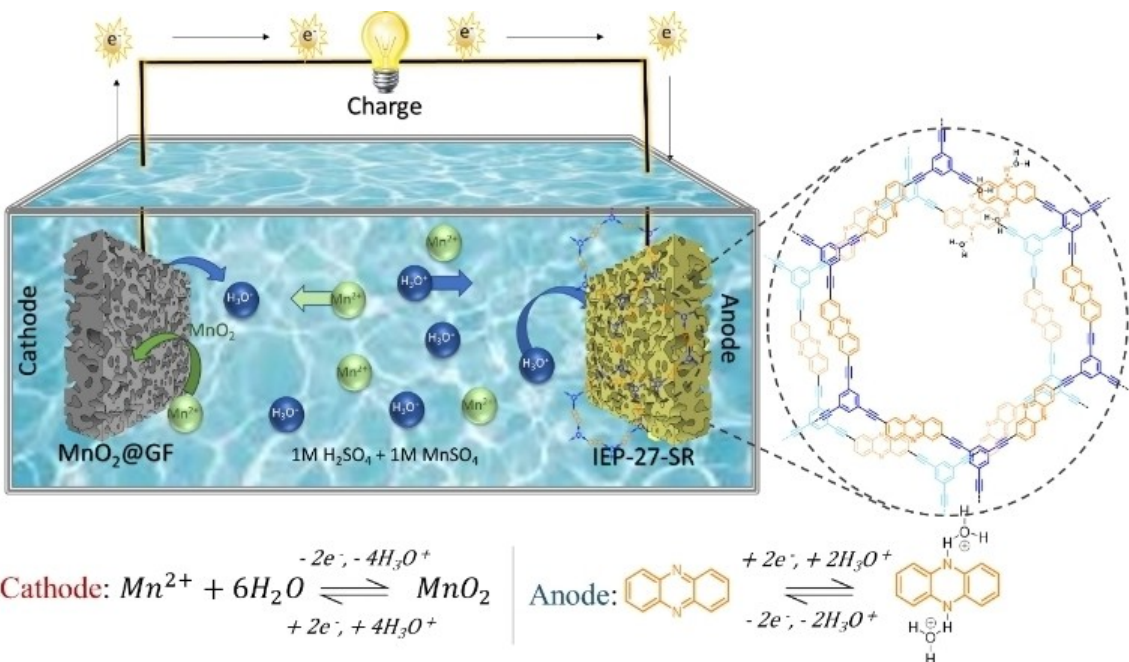
In our previous work,^[35] we demonstrated excellent hydronium-ion storage capabilities of a conjugated phenazine-based microporous polymer (named IEP-27-SR, where IEP stands for Imdea Energy Polymer) in half-cell configurations. Here, we move a step forward by applying our anode (IEP-27-SR) in a real battery, combining it with MnO₂ electrodeposited on graphite felt (MnO₂@GF) cathode in mild acidic electrolyte (1 M H₂SO₄ + 1 M MnSO₄). First, we assessed the fundamental electrochemistry and electrochemical performance of the IEP-27-SR and MnO₂@GF individual electrodes for hydronium-ion storage through a combination of electrochemical techniques, along with *ex situ* SEM-EDS and *ex situ* FTIR measurements. Then, the full cell was assembled with a regular mass loading anode (2 mg cm⁻²) and its rate and long cycling performance were evaluated at various temperatures (from 21 °C to –40 °C). The full cell exhibited not only remarkable cycling stability (83% retention after more than 20000 cycles at 30 °C) but also high-rate capability performance, withstanding up to a high current of 100 C at ambient temperature. Finally, we increased IEP-27-SR loading up to 30 mg cm⁻², reaching an areal capacity of 3.4 mAh cm⁻² at 1 C (4 mA cm⁻²), and the cell still retained a high areal capacity of 2.1 mAh cm⁻² at an exceptional areal current of 10 C (49.4 mA cm⁻²), that is the highest performance reported so far in organic || MnO₂ batteries. With this example, we take a significant step forward in fully harnessing the practicability and sustainability advantages of OEMs for the development of practical batteries.

Results and Discussion

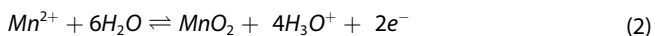
Operating Principle of the IEP-27-SR || MnO₂@GF Battery

A generic scheme of the IEP-27-SR || MnO₂@GF full cell, along with its working mechanism, is shown in Scheme 1. In this battery configuration, MnO₂@GF serves as the cathode, IEP-27-SR acts as an organic anode and an acidic solution containing manganese salt and sulphuric acid (1 M H₂SO₄ + 1 M MnSO₄) acts as the electrolyte. During charge, Mn²⁺ of the electrolyte is oxidised to MnO₂ and deposited on the GF electrode with the generation of H₃O⁺ and electrons that transfer from the positive to the negative electrode via an external circuit. Simultaneously, the IEP-27-SR negative electrode accepts the electrons that convert C=N to C–N[–] functionalities within the phenazine (phz) active units, followed by the coordination of H₃O⁺. During discharge, the opposite reactions occur. The overall mechanism of the redox reaction can be resumed by the following equations.





Scheme 1. Scheme of the IEP-27-SR || MnO₂@GF full cell and redox mechanisms on the anode and cathode sides.



Synthesis and Physicochemical Characterisation of IEP-27-SR Anode

Phenazine-based conjugated microporous polymer hybrid (named IEP-27-SR) was synthesised using a two-step process involving a mini-emulsion and solvothermal reaction (Figure 1a). This synthetic method, consisting of adding nano-carbon additives, namely single-walled carbon nanotubes (SWCNTs) and reduced graphene oxide (rGO), during the miniemulsion step, facilitated the close interaction between the polymer and the carbon nanomaterials as well as the nano-structuring of obtained hybrid (with a final amount of ~10 wt% of nanocarbons), as already demonstrated in our previous works.^[37,39] The chemical composition of the hybrid material was confirmed by solid-state ¹³C NMR (Figures S1a, Supporting Information) and Fourier transform infrared (FTIR) spectroscopies (Figure S1b, Supporting Information), while the presence of carbons was attested by Raman spectroscopy (Figure S1c, Supporting Information). The textural properties of IEP-27-SR were characterized using nitrogen adsorption-desorption isotherm analysis as shown in Figure 1b and c. The isotherm exhibited a type IV shape, which is indicative of mesoporous materials, and the specific surface area (S_{BET}) was measured to be 776 m² g⁻¹. The analysis of the size distribution of the pores revealed the presence of both micropores (51%) and mesopores (46%) with a total pore volume (V_{tot}) of 0.744 m³ g⁻¹ (inset of Figure 1b, Table S1, Supporting Information). Furthermore, the morphology of the polymer particles was examined using field-emission scanning electron microscopy (FE-SEM) and

transmission electron microscopy (TEM). The SEM image (Figure 1d) showed that the polymer particles exhibited a round shape, accompanied by long porous nanowires, resembling a spaghetti-like nanostructure.^[42] Importantly, the inclusion of carbon additives (SWCNTs and rGO) was evident as they surrounded the polymer particles, with SWCNTs exhibiting a wire shape and rGO displaying a wrinkle stack structure. From the TEM image, the particles appeared highly porous, and their size was estimated to be around 400 nm (Figure 1e). Finally, the XRD analysis confirms the amorphous structure of the porous polymer (Figure S1d, Supporting Information).

These characterisation results demonstrate the successful synthesis of the phenazine-based microporous polymer hybrid IEP-27-SR and provide insight into its chemical composition, textural properties, and morphological characteristics as well as a high reproducibility of our synthetic methodology. We urge the readers to follow our previous article for a detailed chemical-physical characterization of the same material.^[35]

Electrochemical Characterization of IEP-27-SR Anode

In our previous work, it was demonstrated that the active phenazine units in IEP-27-SR work by hydronium-ion coordination in 1 M H₂SO₄.^[35] Given the simultaneous presence of two types of cations (Mn²⁺ and H₃O⁺) in the electrolyte of the IEP-27-SR || MnO₂@GF full cell, it becomes crucial to discern and determine which cation is actively participating in the electrochemical redox reactions on the anode side. Therefore, the electrochemical characteristics of the IEP-27-SR buckypaper anode (2 mg cm⁻² polymer mass loading) were evaluated in different hybrid electrolytes, obtained by mixing H₂SO₄ and

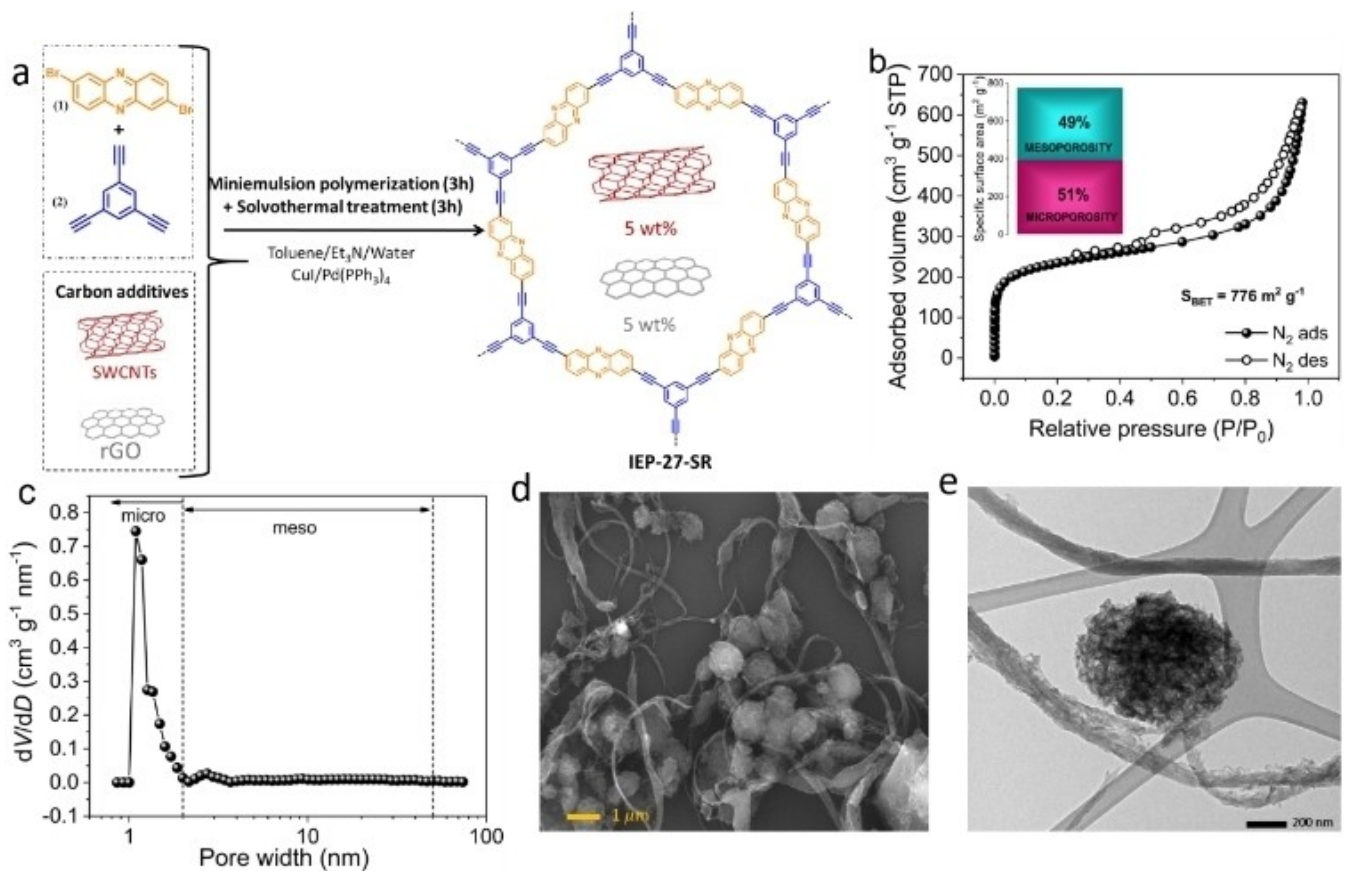


Figure 1. (a) Scheme of IEP-27-SR synthesis, (b) Nitrogen adsorption-desorption isotherm profile with percentages of micro/mesoporosity in inset, (c) Pore size distribution from the quenched solid density functional theory (QSDFT) model, (d) FE- SEM image at 10.000x, 15.0 kV, and (e) TEM image. The scale bar in (d) and (e) is 1 μm and 200 nm, respectively.

MnSO₄ and gradually changing the concentration of one of the salt components and keeping a constant concentration of the other (Figures 2a and S2, Supporting Information).

As is evident in Figure S2, Supporting Information, when the concentration of MnSO₄ increased from 0.1 M to 2 M, keeping constant the concentration of $[\text{H}_3\text{O}^+] = 1 \text{ M}$, no shift in peak position was observed. Differently, when the concentration of Mn²⁺ was kept equal to 1 M and $[\text{H}_3\text{O}^+]$ increased from 0.1 M to 2 M (Figure 2a), the maximum potential shift to more positive values, according to the Nernst equation,^[35] inferring that H₃O⁺ is the charge carrier and not Mn²⁺. To confirm the hydronium-ion coordination mechanism, we performed *in situ* electrochemical quartz crystal microbalance (EQCM) measurements which enables simultaneous recording of mass and charge change (more information about the technique is given in Supporting Information). Through *in situ* EQCM, while processing a CV scan at 3 mVs^{-1} in the potential range of -0.2 to 0.4 V vs Ag/AgCl, the change in frequency was reordered (Figure 2b). The frequency change (increase during reduction and decrease during oxidation) is quite symmetrical, indicating positive and negative mass changes during the reduction and oxidation processes, respectively. Furthermore, it was possible to calculate the slope of the mass change (Δm) versus charge change (ΔQ) in the electrode (Figure 2c), giving, therefore, the estimation of the mass per electron (M. P. E. $\sim 25 \text{ g/mol}$). This value, close to

the theoretical 19 g/mol for one hydronium ion per C=N functionality of PTZ, rather than 1 g/mol for a proton or $\sim 64 \text{ g/mol}$ for Mn $[(\text{H}_2\text{O})_4]^{2+}$, confirms hydronium cycling.^[24]

Moreover, we performed CVs at different scan rates and GCDs at different current rates (C-rates) in three different electrolytes: 1 M H₂SO₄, 1 M MnSO₄ and 1 M H₂SO₄ + 1 M MnSO₄. CVs at various scan rates have similar peak positions and intensities in both 1 M H₂SO₄ and mixed electrolytes (Figures 2d and S3a, Supporting Information). Furthermore, in acid and mixed electrolytes, the CVs show a smaller peak-to-peak separation with comparable values (Figure S4, Supporting Information).^[35] On the contrary, the peak intensity appears lower (Figure S3b, Supporting Information), accompanied by a slightly larger peak separation (106 mV at 2.5 mVs^{-1}) (Figure S4c and d, Supporting Information) when tested in 1 M MnSO₄. This observation suggests a distinct and inferior redox activity of IEP-27-SR in this electrolyte, as confirmed by the low capacities obtained in GCD experiments (Figure S5a, Supporting Information). In contrast, similar charge-discharge profiles with high capacities (Figures 2e and S5b, Supporting Information) and capacity retentions (rate experiment) (Figure S6, Supporting Information) were obtained in 1 M H₂SO₄ and mixed electrolytes. The IEP-27-SR buckypaper electrode could reach a high value of capacity of 118 mAh g^{-1} at 2 C (where 1 C = 194 mA g^{-1} , calculated considering the sole mass of the polymer, excluding

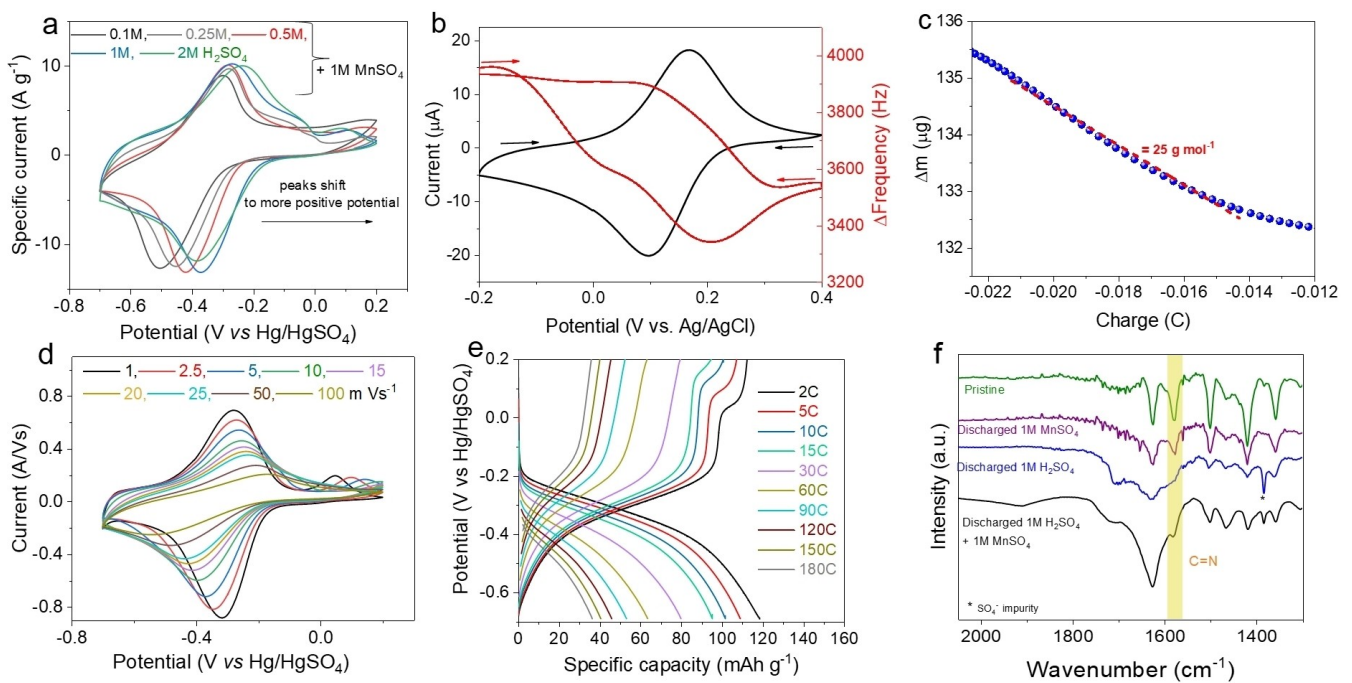


Figure 2. Electrochemical characterization of IEP-27-SR anode. (a) CVs in electrolytes 0.1–2 M H₂SO₄ + 1 M MnSO₄ electrolytes, (b–c) in-situ EQCM measurements: (b) Cyclic voltammetry of the crystal quartz electrode IEP-27-SR in 1 M MnSO₄ + 1 M H₂SO₄ recorded at 3 mV s⁻¹, and correspondent frequency change response as recorded. (c) Mass change vs corresponded charge in the reduction range of the CV. (d) CVs at different scan rates in 1 M H₂SO₄ + 1 M MnSO₄. Current are normalized respect to the applied scan rate. (e) GCDs at different current rates in 1 M H₂SO₄ + 1 M MnSO₄, and (f) ex situ FTIR of the pristine (green), discharged in 1 M MnSO₄, (purple line), in 1 M H₂SO₄ (blue line) and in 1 M H₂SO₄ + 1 M MnSO₄ (black line) IEP-27-SR electrodes.

the carbon contribution) and still maintained 64 mAh g⁻¹ (54% retention) at a high C-rate of 60 C in the mixed electrolyte (Figure 2c). Moreover, IEP-27-SR cycled stably without capacity attenuation over 450 cycles at 10 C (Figure S7, Supporting Information), confirming the high stability and fast kinetics of our polymer in the mixed electrolyte. A similar capacity value (122 mAh g⁻¹) was obtained in 1 M H₂SO₄ (Figure S5b, Supporting Information). In contrast, only a small capacity of 15 mAh g⁻¹ was obtained at the same current density of 2 C in 1 M MnSO₄, suggesting that there was insufficient activity of Mn²⁺ for the underlying redox reactions (Figure S5a, Supporting Information). These results demonstrate that the hydronium ions are the principal charge carriers promoting the excellent redox activity of IEP-27-SR in the mixed electrolyte.

According to the redox mechanism (Equation 1), when phenazine active units (phz) are reduced (during battery charge), a dianion is formed (phz²⁻), followed by coordination with the cations for charge compensation.^[35,43] In order to confirm this redox mechanism and clarify the charge carriers, FTIR spectra (Figure 2f) and ex situ SEM-EDS (Figure S8, Supporting Information) mapping were obtained for discharged/charged electrodes in 1 M H₂SO₄, 1 M MnSO₄, and mixed electrolytes. Ex situ FTIR of the pristine electrode shows a prominent peak at 1590 cm⁻¹, which corresponds to the C=N bond of the active phenazine unit, that becomes significantly less pronounced after being reduced in acid and mixed electrolytes. In contrast, this band almost retained its intensity when the reduction was carried out in 1 M MnSO₄, which confirms the decreased redox activity of IEP-27-SR in the non-

protic electrolytes.^[35] Regarding the counter-cation, if hydronium ions are the principal charge carriers in the mixed electrolyte, the fraction of Mn²⁺ cations should be minimal or absent in the discharged electrode (reduced). The EDS elemental mapping of the IEP-27-SR electrodes; pristine (Figure S8a, Supporting Information), fully charged (oxidized; Figure S8b, Supporting Information), and fully discharged (reduced; Figure S8c, Supporting Information) in the hybrid electrolyte, evidenced the negligible presence of Mn. In contrast, a small yet visible amount of Mn (0.4 wt.%) was detected in the electrode that was reduced in 1 M MnSO₄, where Mn²⁺ is the sole cation present (Figure S8d, Supporting Information). It is worth noting that this low presence of Mn is associated with the poor redox activity of IEP-27-SR electrodes in this electrolyte.

These preliminary results corroborate the redox mechanism of phenazine units in the presence of H₃O⁺, which is consistent with previous literature reports for a similar family of building blocks, such as HATN,^[24,33] and DPPZ.^[44] Moreover, it has been demonstrated that the presence of Mn²⁺ in the electrolyte does not affect the electrochemical behavior.

Kinetic Analysis: Hydronium Diffusion Kinetics in the IEP-27-SR Anode

The electrochemical kinetics of the redox reactions in the polymer anode were investigated by potentiostatic electrochemical impedance spectroscopy (PEIS) and galvanostatic

intermittent titration technique (GITT) (Figure 3). Two electrodes cells, combining IEP-27-SR with oversized activated carbon (AC) and using 1 M H₂SO₄ as electrolyte were employed. First, PEIS measurements were carried out at different potentials (from -0.25 V to 0.5 V), and temperatures (from +25 to -10 °C). All Nyquist plots feature two regions: a depressed semicircle attributed to the charge-transfer process in the high-frequency region and an inclined line in the low-frequency region corresponding to the diffusion (Figures 3a and S9a, Supporting Information). The fitting of the semicircle is represented in Figure S10, Supporting Information, and the Nyquist plots and the calculated charge transfer resistance (R_{CT}) and equivalent series resistance (R_s) at each potential are given in Figure S9b and c, Supporting Information. The R_s value remains fairly constant around 0.23 Ω, and R_{CT} values were found to be small, ranging from 0.65–1 Ω, with a small increase/decrease observed during charge (polymer oxidation)/discharging (reduction of

the polymer). Furthermore, only a very small increase in R_{CT} with the decrease in temperature was noted (Figure 3a). Noticeably, the activation energy for the charge transfer parameter (E_a, R_{CT}) calculated using the negative slope of the Arrhenius plot, was found to be extremely small, i.e., 1.5 kJ mol⁻¹ (Figure 3b), combinedly emphasising the facilitated hydronium-ion mobility through the electrode/electrolyte interface.

Second, GITT test was conducted to extract information about hydronium-ion diffusion ($D_{H_3O^+}$) within the bulk of IEP-27-SR (Figure 3c). $D_{H_3O^+}$ average values of 0.9×10^{-6} and 2.88×10^{-6} cm² s⁻¹ were obtained for charging and discharging cycles, respectively. These values are remarkably high compared to that reported for organic hydronium-ion batteries that commonly ranges 10^{-10} – 10^{-13} cm² s⁻¹.^[31] GITT was also conducted at different temperatures (from 25 °C to -10 °C) to obtain the activation energy for hydronium diffusivity ($E_a, D_{H_3O^+}$) applying the Arrhenius equation (Figures 3d and S11, Support-

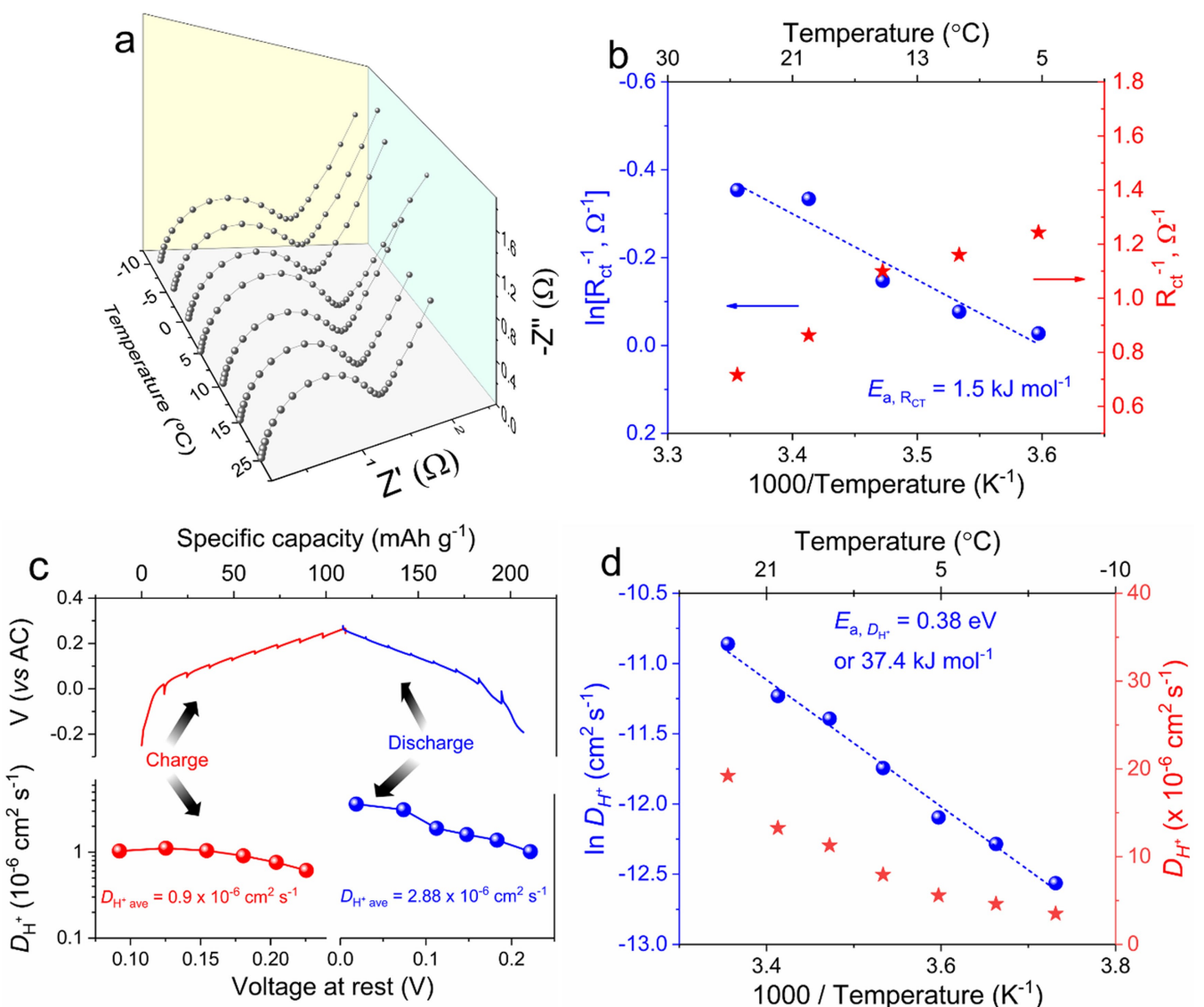


Figure 3. Electrochemical kinetic evaluation of hydronium-ion storage in IEP-27-SR anode. (a) PEIS Nyquist plots at different temperatures, (b) temperature dependence of R_{CT} and activation energy for R_{CT} calculated by the Arrhenius law, (c) GITT curves (upside) and hydronium-ion diffusivity ($D_{H_3O^+}$) (down side), (d) temperature dependence of $D_{H_3O^+}$ (red stars) and activation energy for $D_{H_3O^+}$ (blue dots) calculated by the Arrhenius law.

ing Information). The low value obtained, 0.38 eV (37.4 kJ mol⁻¹), demonstrates a unique method of conduction manner *via* the Grotthuss-type mechanism ($E_a < 0.4$ eV),^[45] where hydronium transfer could occur by forming/breaking of hydrogen bonds between adjacent phenazine groups, despite the rigid nature of the CMP. This conduction mechanism is much more facile in comparison to the conventional diffusion mode, enabling fast kinetics.

In summary, the facile charge transfer process (low R_{CT} and low E_a , R_{CT}) and the facilitation of the diffusivity of the hydronium diffusivity (high $D_{H_3O^+}$ and low E_a , $D_{H_3O^+}$) within the IEP-27-SR anode, should impart high rate performance in the IEP-27-SR | MnO₂@GF full battery.

Electrochemical Characterisation of MnO₂@GF

The Mn²⁺/MnO₂ redox reaction relies on the deposition of Mn²⁺ in the graphite felt (GF) as MnO₂ during the charge, with the concomitant release of hydronium ions. Conversely, during discharge, this process is reversed, leading to the release of Mn²⁺ ions back into the electrolyte solution (Equation 2). As already demonstrated,^[46] the presence of hydronium ions in the electrolyte is fundamental since it promotes the dissolution of MnO₂ in the discharge process and reduces the cell overpotential. However, excessively high concentrations of hydronium ions can stabilize the Mn³⁺ intermediate that has enough time to diffuse away from the GF causing a decrease in the discharge capacity.^[47] After screening different compositions (see explanatory note in Figure S12a, Supporting Information), we selected 1 M H₂SO₄+1 M MnSO₄ to investigate the reversibility of the Mn²⁺/MnO₂ reaction on graphite felt. Further discussion about the Mn²⁺ plating/stripping electrochemistry is given in Figure S12, Supporting Information.

Then, we used the same electrolyte formulation to prepare electrodeposited MnO₂ on GF that will be further used as cathode (MnO₂@GF) in the full battery. It is important to note that the pre-deposition treatment of MnO₂ was implemented to mitigate the small variation in Coulombic efficiencies observed between the anode and cathode during the initial cycles. Pre-electrodeposited MnO₂ on GF (MnO₂@GF) samples were obtained by applying a constant current of 5 mA cm⁻² and limiting the deposition capacity to 1, 5 and 10 mAh cm⁻² at ambient conditions. Consistent with previous studies,^[48] FE-SEM images (Figure S13, Supporting Information) show that at a low deposition capacity of 1 mAh cm⁻², the MnO₂ deposited was insufficient to fully coat the surface of the GF, while at a high deposition capacity of 10 mAh cm⁻², the MnO₂ layer grows irregularly. SEM-EDS elemental mapping images confirm that MnO₂ is uniformly distributed with Mn and O elements homogeneously distributed throughout the GF surface at an intermediate deposition capacity of 5 mAh cm⁻² (see Figure S14, Supporting Information and related explanatory note). Raman spectroscopy (Figure S15a, Supporting Information) further corroborates that 1 mAh cm⁻² deposition capacity is not sufficient to homogeneously cover the GF surface since the GF peaks are still present in the spectra. Differently, no carbon

peaks are visible in the case of 5 mAh cm⁻² MnO₂@GF and three intense peaks attributed to MnO₂ appear at the low frequency region, validating the precedent observations. Finally, XRD patterns of the electrodeposited MnO₂@GF samples (Figure S15b, Supporting Information) showed distinct diffraction peaks corresponding to the Akhtenskite phase (identified using the JCPDS 30-0820 reference), that is, the common phase observed for electrodeposited ε-MnO₂.^[13,22,27] Based on these analyses, we selected 5 mAh cm⁻² MnO₂@GF as our optimal cathode for the full cell.

Electrochemical Performance of IEP-27-SR | MnO₂@GF Full Cell

Full Cell Assembly and Working Mechanism

After investigation of single electrodes, the IEP-27-SR | MnO₂@GF full batteries were assembled according to Scheme 1, in which IEP-27-SR buckypaper and MnO₂@GF electrode were used as anode and cathode, respectively, with a mixed electrolyte (1 M H₂SO₄+1 M MnSO₄). Figure 4a shows the CV curves of the individual electrodes and of the full cell recorded at 1 mVs⁻¹. Galvanostatic charge-discharge experiments (Figure S16, Supporting Information) revealed that the average discharge voltage is around 0.9 V with maximum specific capacities of 101 mAh g⁻¹ at 2 C. This value is in good agreement with the value anticipated from the potential difference between the anode and cathode pairs (~0.98 V). The low CE observed at this low rate (~88%) is likely due to the combination of certain HER in the anode and mainly to the intrinsic sluggish efficiency of the deposition/dissolution process of Mn²⁺ on GF, as reported elsewhere.^[47] Nevertheless, the CE% increased and remained stable around 98–99% beyond 5 C (Figure 4b and c). With increasing C-rates, the capacity decreased monotonically, as commonly observed for battery materials. It is worth noticing that, at the high current density of 20 C (which corresponds to a discharge time of only 1.4 minutes), the capacity retention is still as high as 75%, yet achieving 41 mAh g⁻¹ at an extreme 100 C rate, highlighting superior rate capability of the demonstrated battery.

The electrochemical kinetics of the IEP-27-SR | MnO₂@GF full cell was further investigated by CV at different scan rates (v) (Figure 4d). First, a Laviron analysis was performed to obtain the kinetic parameters, α and k^0 , which were calculated to be $\alpha = 0.50$ and $k^0 = 0.18$ s⁻¹ (Figure S17a, Supporting Information). These results indicate good symmetry of the electron transfer energy barrier of the redox reactions and fast kinetics in the full battery, respectively. Second, a power law analysis was applied to calculate the b value (see Equations S5 and S6 given in Supporting Information). An ideal b -value of 0.5 indicates a diffusion-controlled process, while a b -value of 1.0 signifies a capacitive-controlled behaviour. The oxidation and reduction peaks of IEP-27-SR | MnO₂ show high b -values of 0.82/0.89 for the anodic/cathodic peaks, respectively, indicating that the overall redox response tends to be more capacitive-controlled (Figure 4e). Finally, following the Dunn method (see Equa-

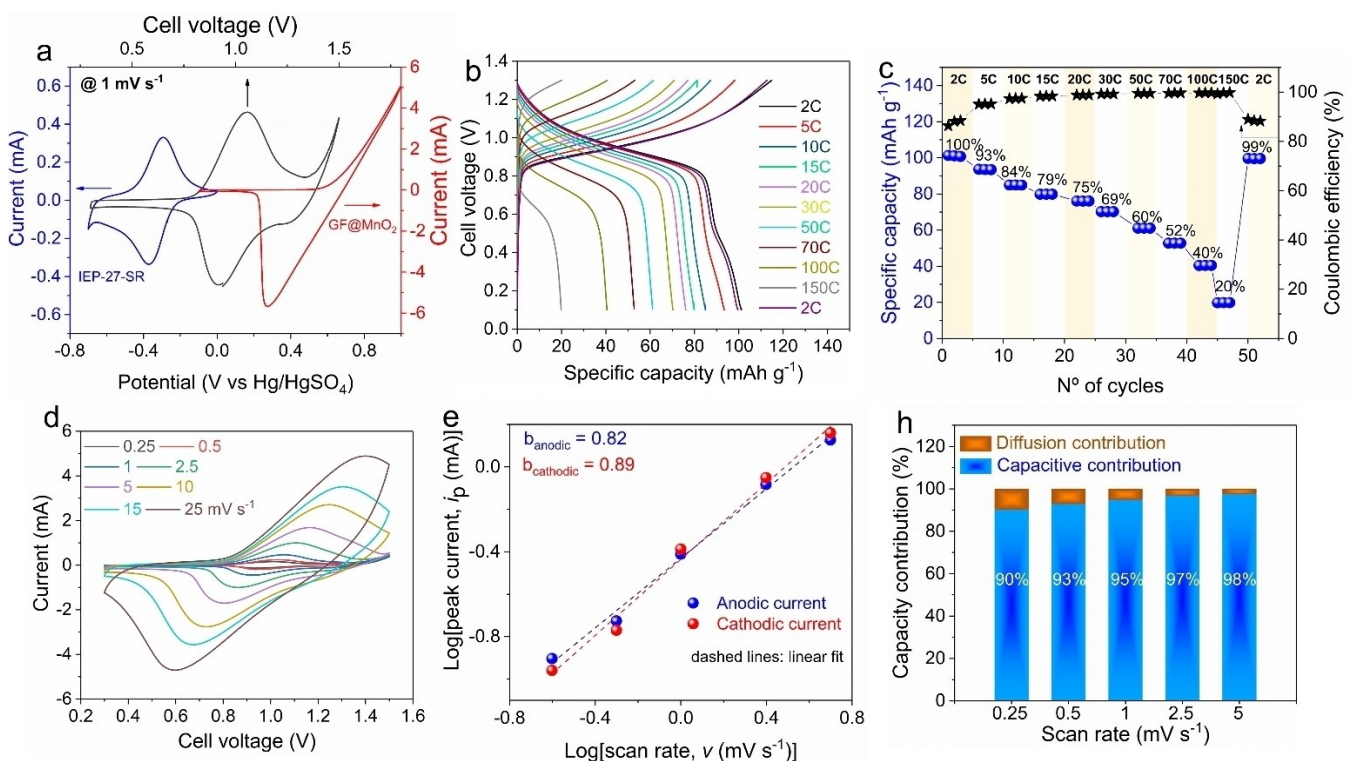


Figure 4. IEP-27-SR || MnO₂@GF full cell performance. (a) CVs of the anode, cathode, and full cell recorded at 1 mV s⁻¹, (b) rate GCD profiles at different C-rates, and the corresponding capacities (c). Specific capacity vs. number of cycles and CE% and respective capacity retentions (%). (d) CVs of the full cell at different scan rates and the corresponding power-law analysis. (e) Capacitive and diffusion contributions are calculated by applying the Dunn method (f).

tions S7 and S8 in Supporting Information), we determined quantitatively the contribution of capacitive and diffusion dependent on the rate to the current response.^[49] As shown in Figure 4f, even at the slowest scan rate of 0.25 mV s⁻¹, the capacitive contribution to the overall capacity is remarkably high, accounting for 90% of the total capacity. When the scan rate is increased to 5 mV s⁻¹, the capacitive contribution further increases to 97.6%, aligning with expectations, since the fraction of capacitive contribution increases with the increase of scan rate (Figure S17b, Supporting Information). This capacitive-dominated behavior of IEP-27-SR is consistent with the high b-values observed for both the anodic and cathodic peak currents, confirming the rapid kinetics of the underlying redox reactions in the porous polymer anode.

Ultrafast-Charge Capability of IEP-27-SR || MnO₂@GF Full Cell

Based on the observed fast-redox kinetics, we tested the full cell as an ultrafast charging battery. First, by applying constant current (CC), galvanostatically, we charged (CC-cha) our battery at different C-rates (from 2 C up to 20 C) and then discharged (CC-dis) at a fixed 2 C (Figure 5a). Although the discharge capacities dropped from 90 to 78 mAh g⁻¹, when we increased the charging rates from 2 C to 20 C, the loss in capacity was only 12 mAh g⁻¹. Referring to charging time, 10 C and 20 C charging enable 2.5 and 1.15 min of rapid charging (Figure S18, Supporting Information), still delivering 80 and 73% (with

respect to discharge capacity at 2 C charging) discharge capacities, respectively (Figure 5b).

Finally, we aimed to demonstrate the rapid charging capability of our battery in just a few seconds, using a specific method in which we keep the voltage constant while charging (CV-cha) and control the galvanostatic current while discharging (CC-dis).^[52,53] Although CV charging, applied for a short duration, enables significantly faster charging times compared to using CC alone, it is less explored for organic batteries.^[25] Figure 5c shows a typical CV-cha curve at 1.3 V that drained an immense initial specific current of 70.95 A g⁻¹, before rapidly decaying to 0.16 A g⁻¹. The full cell was charged 50 and 80% in 8 and 18 s, respectively, and assumed to be fully charged to its maximum achievable capacity of 104 mAh g⁻¹ after 75 s. Furthermore, to estimate discharge capacity after applying CV-cha, CC-dis was used at different C-rates (Figure S19, Supporting Information). At 2 C CC-dis, the full cell delivered a higher capacity of 104 mAh g⁻¹ (versus 78 mAh g⁻¹ which approximately corresponds to 20 C CC-cha as described in the context of Figure 5a). Additionally, with increasing C-rates, the discharge capacities obtained by applying this extreme protocol are still notable. Nevertheless, both the CC-cha and CV-cha protocols demonstrate the feasibility of ultrafast charge capability of the full cell, particularly the CV-cha mode that can withstand variable and high specific charging currents without penalising much discharge performance. Both the anode and cathode components of the demonstrated full cell have been designed to sustain high currents, thanks to their fast reaction kinetics, as

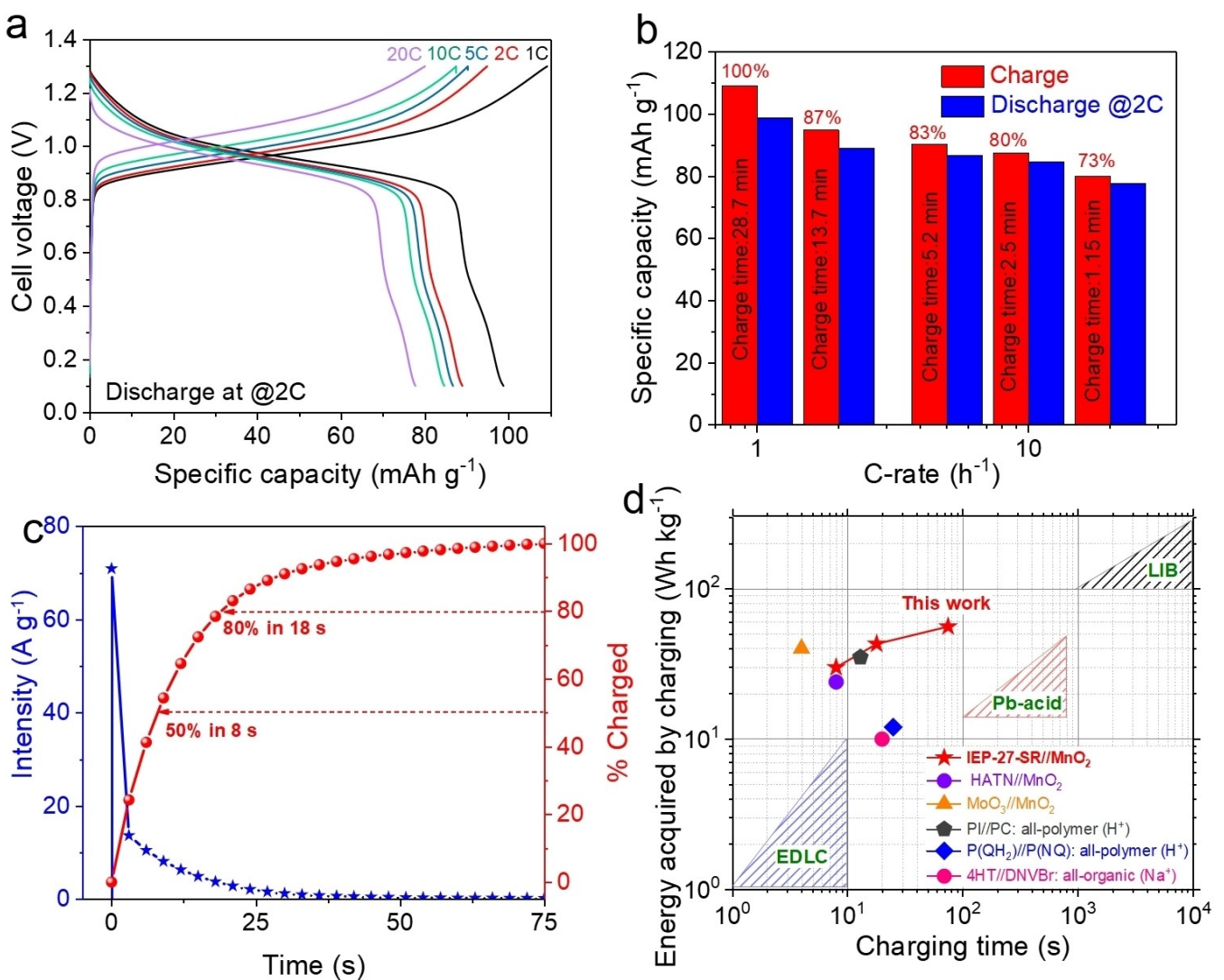


Figure 5. Ultrafast-charging of IEP-27-SR | MnO_2 @GF full cell. (a) GCD curves of the full cell charged at different C-rates and discharged at 2 C, and the corresponding specific capacities, along with charging time at each C-rate (b). (c) A typical current intensity vs charging time and % charged obtained by constant voltage (CV) charging (CV-cha) at 1.3 V. (d) Merits of fast charging electrochemical energy storage systems. A brief summary of energy acquired by charging versus charge time for different energy storage systems. HATN// MnO_2 ,^[24] MoO_3 // MnO_2 ,^[18] PI//PC: all-polymer (H^+),^[50] P(QH_2)//P(NQ): all-polymer (H^+),^[25] 4HT//DNVBr: all-organic (Na^+).^[51]

detailed in sections 2.4 and 2.5, respectively. To provide a perspective on ultrafast charging capacity, we compared energy (based on the total weight of both electrodes) acquired by charging with charging time (Figure 5d). Unsurprisingly, the charging time for this full cell is shorter (and longer) with lower (and higher) energy than state-of-the-art LIBs (and EDLCs), respectively. In addition, faster charging is attained compared to that of Pb-acid batteries with comparable energy values. Both energy and charging time are beneficial compared to some of the best-performing all-organic (or polymer) aqueous batteries.^[24]

Cycle Stability of IEP-27-SR | MnO_2 @GF Full Cell

After elucidating the excellent rate performance, we tested the full cell for long-term cycling stability by applying the CC-cha/CC-dis protocol (Figures 6a and S20a, Supporting Information). The full cell demonstrated an ultralong life span; retaining a remarkable 91% and 83% initial capacity over extended 10000 and 20400 cycles, respectively, which correspond to 490 hours of cycling at 30 C. In terms of capacity loss, it was only $0.65 \mu\text{Ah g}^{-1}$ per cycle or $27.2 \mu\text{Ah g}^{-1}$ per hour. It is also worth mentioning here that after the initial few cycles, the CEs remain above 99% with an average value of 99.5% over the entire cycling period.

We also cycled the cell by applying the CV-cha/CC-dis (at 30 C) protocol (Figures 6b and S20b, Supporting Information). Under these harsh testing conditions, the cell retained an

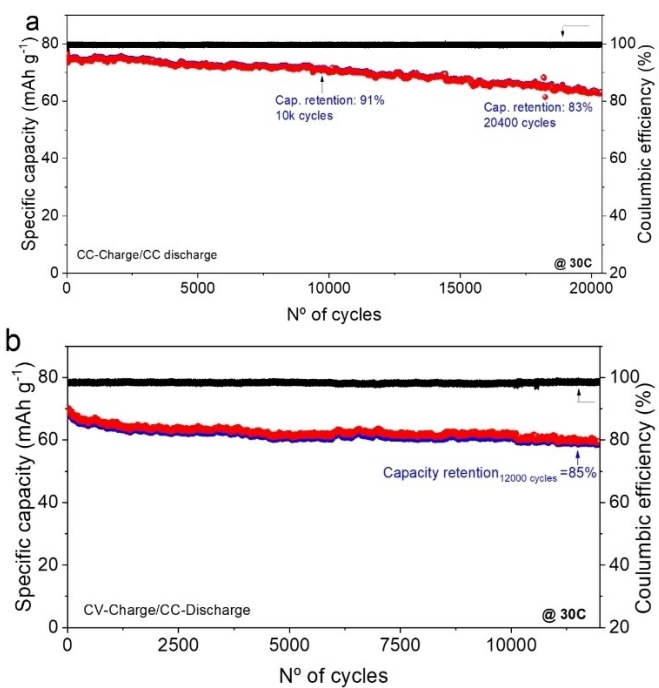


Figure 6. Long-term cyclability of IEP-27-SR | MnO₂@GF full cells, applying CC-cha/CC-dis at 30 C (a) and CV-cha (1.3 V, 150 s/0.116 mAh: limiting time/capacity)/CC-dis (at 30 C) (b) protocols.

impressive 85% capacity over 12000 cycles, with a small capacity loss of 0.67 $\mu\text{Ah g}^{-1}$ per cycle or 12.9 $\mu\text{Ah g}^{-1}$ per hour (total cycling period of 627 hours).

It is important to note that the MnO₂@GF cathode was not replaced during both the cycling tests. This stable-cycling experiment in the mixed electrolyte can be at least, partly, associated with the high robustness of our conjugated micro-porous polymer anode, which we have already demonstrated in our previous article, but in the presence of hydronium-ions, only.^[35]

Low-T Operativity

Because acidic electrolytes have a low freezing point, we decided to explore the possibility of using this cell in low-temperature conditions. For this purpose, we increased the H₂SO₄ concentration to 3 M, to further decrease the freezing point.^[30]

We gradually decreased the temperature from 21 °C down to -40 °C and evaluated the performance of the cell at each temperature. Figure 7a collects the GCD profiles at different temperatures recorded at 1 C. As the temperature was reduced, as expected, the specific capacity values decreased with a concomitant increase in voltage polarisation. However, even at the lowest tested temperature of -40 °C, the cell exhibited a reasonable specific capacity of 63 mAh g⁻¹ (58% compared to the capacity at 21 °C), indicating its effectiveness under harsh cold conditions. We also investigated the GCD performance of our cell by progressively lowering the temperature and increasing the C-rates (rate capability test for each temperature, Figures 7b and S21, Supporting Information). Once again, both the specific capacity and the rate capacity decreased monotonously with the decrease in temperature (Figure S22a and b, Supporting Information). Interestingly, a high specific capacity of 79 mAh g⁻¹ is still obtained at -20 °C at 1 C, and yet 40 mAh g⁻¹ at 20 °C, indicating still good rate capability at reduced temperatures as well. Understandably, the decreased performance at low temperatures can be linked to the aggravated polarisation on account of increase of R_{CT} and reduction of $D_{H_3O^+}$ within the bulk of IEP-27-SR as decreasing temperature which limits electrode capacity utilization and rate performance.

A representative low-T cycling experiment was also carried out at -30 °C at 5 C (Figure S22c, Supporting Information). The cell revealed still decent capacity (around 55 mAh g⁻¹) and good capacity retention of 93% after 1500 cycles with quantitative CEs.

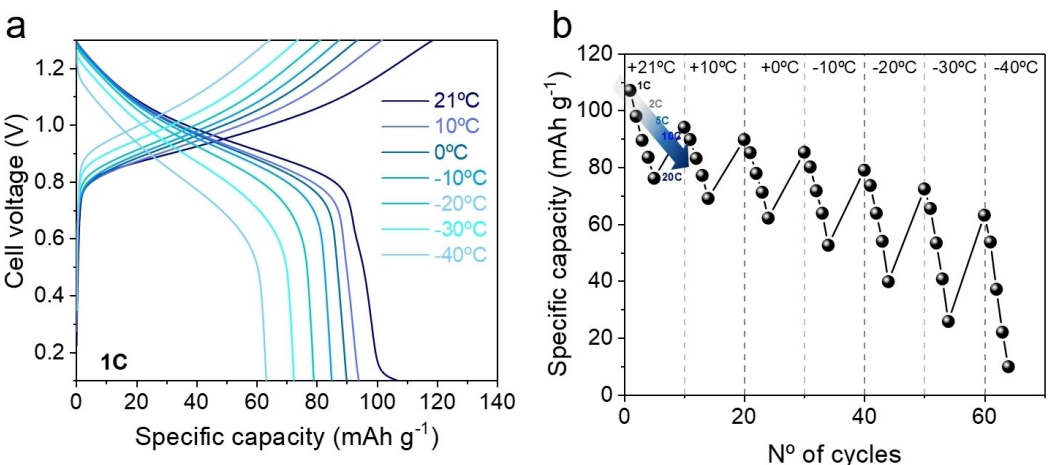


Figure 7. Low-temperatures operativity of IEP-27-SR | MnO₂@GF full cell in 3 M H₂SO₄ + 1 M MnSO₄. (a) Some representative GCD profiles recorded at 1 C at different temperatures (from +21 °C to -40 °C). (b) Specific capacity recorded at different C-rates (from 1 C to 20 C) and at different temperatures.

High-Mass-Loading Polymer Anodes

We previously emphasized the development of thick or high mass loading organic electrodes, together with a high polymer fraction, leading to large areal capacities beyond 3 mAh cm^{-2} ^[39]. In this scenario, organic electrodes can increase the competitiveness of practical batteries, thus fully exploiting their intrinsic cost and sustainability advantages. As mentioned in the introduction, most of the reported organic MnO₂ batteries employed low mass loading organic anodes, typically below 3 mg cm^{-2} (Table S2, Supporting Information) with reasonable polymer content on the electrode (commonly, 50–70 wt%), resulting in nonpractical areal capacities. To address these issues, we fabricated thicker electrodes, increasing the active mass loading from 2 mg cm^{-2} to 30 mg cm^{-2} (see Figure S23, Supporting Information for their digital images and thickness information). It is worth highlighting once again here that the nonactive components in the electrode anode are only 20 wt% (that means that only 10% of carbon is added to the hybrid) for all the electrodes, meaning that the active-polymer content is as high as 80 wt%.

Figure 8 illustrates the electrochemical performance of IEP-27-SR| |MnO₂@GF full cells with anodes of different mass loadings (voltage profiles in Figure S24, Supporting Information). The increase in voltage polarization appears to be small with increasing anode mass loading, at least at 2 C (Figure 8a). Therefore, the gravimetric capacities at 2 C remained high in

the range of $100\text{--}110 \text{ mAh g}^{-1}$, whereas the areal capacities were scaled proportionally to the anode mass loading (Figure 8b).

The rate capability followed a common trend (Figures 8c and d and S25, Supporting Information). As both mass loadings and C-rates (or areal currents) increased, capacities (both gravimetric and areal) and capacity retention (capacities at higher C-rates compared to 1 C) decreased monotonically. This decrease was more pronounced in high-mass-loading electrodes, particularly at higher C-rates. Despite this trend, the full cell with a high IEP-27-SR anode mass loading of 30 mg cm^{-2} still showed an impressive areal capacity of 3.4 mAh cm^{-2} at the C-rate of 1 C (Figures 8d and S25a Supporting Information). In comparison, an anode with a low mass loading of 2 mg cm^{-2} achieved only 0.2 mAh cm^{-2} (17 times smaller) areal capacity under the same conditions. Furthermore, when the C-rate reached the high value of 10 C, all cells showed good value of capacity retention, even in the case of thicker polymer anodes (75% and 62% for 20 and 30 cm^{-2} , respectively), despite 133 and 167-fold areal current enhancements (Figures 8d and S25b, Supporting Information). Furthermore, the full cell with 20 mg cm^{-2} anode mass loading still revealed good capacity retention of 87% after 300 repeated GCD cycles at 5 C (19.25 mA cm^{-2}), while maintaining CEs greater than 99%, as evidenced in Figure S26, Supporting Information.

Finally, in Figure 8e and f, we compared the performance of our full cell with the reported best performing organic| |MnO₂

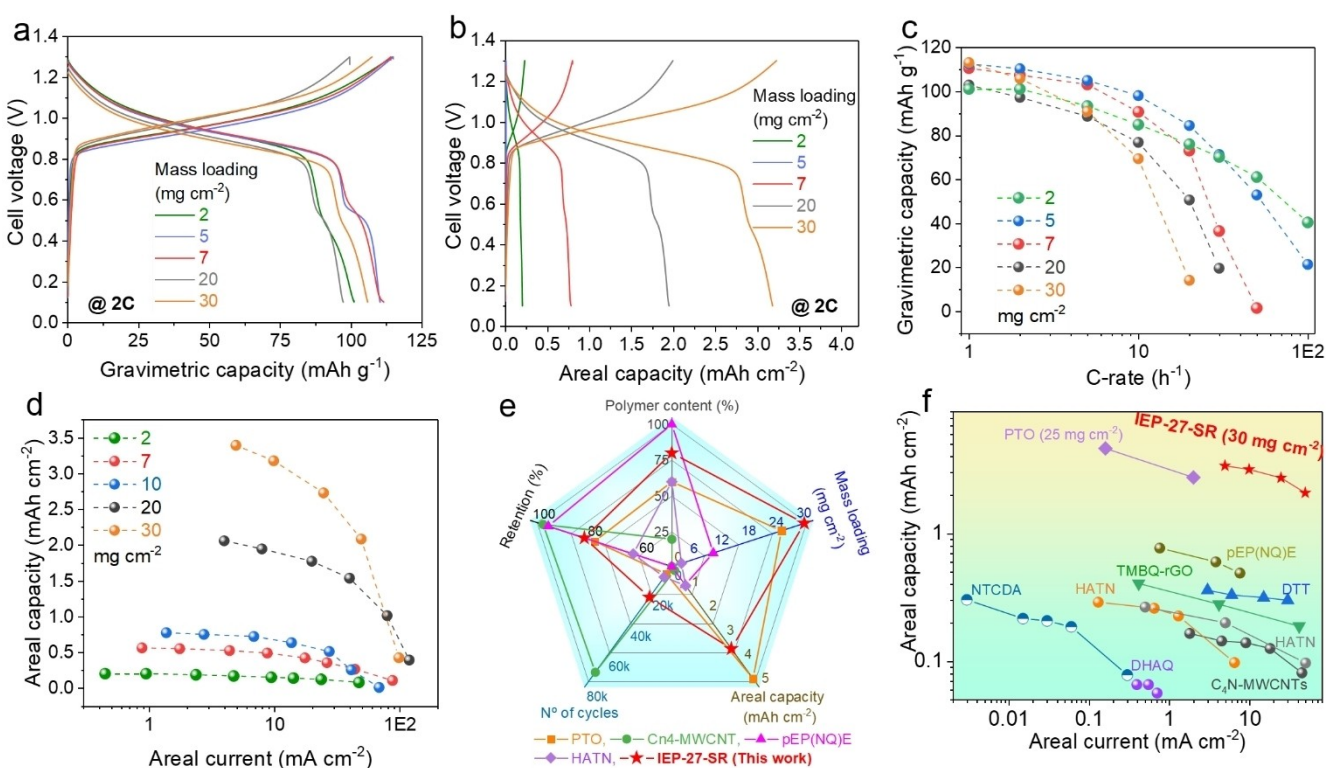


Figure 8. Performance evaluation of the IEP-27-SR | | MnO₂@GF full cell at different polymer anode mass loadings in 1 M H₂SO₄ + 1 M MnSO₄. Representative GCD cell voltage-gravimetric (a) and areal (b) capacity profiles at 2 C. Gravimetric (c) and areal (d) rate capability. (e, f) Comparison of the full cell performance with the state-of-the-art organic | | MnO₂ batteries-areal capacity vs areal current (all the examples are reported in Table S2) (e) and Radar plot summarizing various performance metrics. The literature examples are PTO,^[48] C4n-MWCNTs (50%),^[30] pEP(NQ)E,^[29] NTCDA,^[27] HATN,^[33] DTT,^[31] TMBQ-rGO,^[22] DHAQ molecule^[54] and HATN.^[24]

batteries, even if we are aware that electrode composition, electrolyte concentrations, and sometimes, set-ups are different, so a completely fair comparison is difficult to accomplish. All electrochemical performance metrics, including other reported examples, are given in Table S2, Supporting Information.

Among the state-of-art examples of organic| MnO_2 , tetramethylquinone (TMBQ)| MnO_2 , demonstrated the highest specific capacity (320 mAh g^{-1}) combined with good cycle stability (77% capacity retention after 4000 cycles).^[22] However, the content of active material in the anode (60 wt.%) and its mass loading (1.27 mg cm^{-2}) are too low for practical batteries, where areal capacities $> 3 \text{ mAh cm}^{-2}$ are required. Oka et al. reported an electropolymerized pEP(NQ)E anode with a mass loading of 10 mg cm^{-2} . This active mass loading can potentially increase the areal capacity values, but unfortunately, the specific capacity and cycle stability were limited to 76 mAh g^{-1} and 50 cycles, respectively.^[29] Gua et al.,^[48] pushed the mass loading barrier to 25 mg cm^{-2} , reaching a high areal capacity of 4.6 mAh cm^{-2} at a low current with the pyrene-4,5,9,10-tetraone (PTO)| MnO_2 system. However, the capacity dropped to 3.25 mAh cm^{-2} when the areal current increased to 2 mA cm^{-2} and higher currents were not reported. Although Yang et al.,^[30] described a microporous C₄N/multi-walled carbon nanotubes-50% composite| MnO_2 with unprecedented cycle stability (98% capacity retention after 11000 cycles) in a highly concentrated acidic electrolyte ($5 \text{ M H}_2\text{SO}_4 + 0.5 \text{ M MnSO}_4$), the low polymer content (30 wt.%) and low active mass loading electrodes (0.9 mg cm^{-2}) resulted in low areal capacities.

In this work, our IEP-27-SR battery not only showed notable capacity retention during long cycling (84% after 20400 cycles) but also, thanks to high polymer content (80 wt.%) and high mass loading (30 mg cm^{-2}) in the anode, our full cell reached the high areal capacity value of 3.4 mAh cm^{-2} , that is among the highest reported so far for organic| MnO_2 batteries (Figure 8e). Furthermore, our high mass loading cell was also able to sustain a high value of areal currents, while maintaining a notable areal capacity of 2 mAh cm^{-2} even under the extremely high areal current of 50 mA cm^{-2} , never reported thus far for such systems (Figure 8f). This comparison unleashes its superiority to deliver high capacities and large power, simultaneously under practically relevant conditions.

Conclusions

In this study, we successfully developed a high-performance polymer-Mn acid battery utilizing hydronium-ion coordination/un-coordination on the anode consisting of phenazine-conjugated microporous polymer (IEP-27-SR) and the $\text{Mn}^{2+}/\text{MnO}_2$ conversion reaction on the $\text{MnO}_2@\text{GF}$ cathode. The IEP-27-SR anode, characterized by enhanced structural/morphological features, such as high BET specific surface area, mixed micro-/mesoporosity, nanostructurization, and hybridization, facilitated rapid hydronium ion mobility. Consequently, the IEP-27-SR| $\text{MnO}_2@\text{GF}$ full cell demonstrated a discharge capacity of 101 mAh g^{-1} at 2 C, excellent rate performance of 41 mAh g^{-1} at 100 C, and operability at low temperatures (63 mAh g^{-1} at

-40°C) with a regular polymer mass loading of 2 mg cm^{-2} , despite an 80 wt% content. In addition, the full cell exhibited ultrafast charge capability, achieving 80% quick chargeability in 18 seconds in potentiostatic mode, while maintaining a high discharge capacity of 104 mAh g^{-1} . The robust 3D architecture of the porous polymer anode contributed to impressive cycling stabilities, with 83% and 85% capacity retentions over 20400 and 12000 cycles using conventional galvanostatic and stringent potentiostatic charging modes, respectively. Furthermore, the practicality of the organic electrode was demonstrated with a high mass loading polymer anode (30 mg cm^{-2}), which leads to a full cell with a high areal capacity of 3.4 mAh cm^{-2} . Even with an extremely high areal current (50 mA cm^{-2}), it retained 2 mAh cm^{-2} . This concurrent high performance represents a significant advance in this cell chemistry, suggesting potential applications for designing safe, sustainable, and advanced rechargeable acid batteries.

Supporting Information Summary

Supporting table, figures and equations are in Supporting Information file.

Acknowledgements

Authors thank the European Union's Horizon 2020 research and innovation programme under the Marie Skłodowska-Curie Grant agreement (Grant No 860403) and Spanish Government; MICIU/AEI/10.13039/501100011033 and by the European Union NextGenerationEU/PRTR (PID2021-124974OB-C21 and PID2019-106315RB-I00) for the funding. NP appreciates fellowship IJC2020-043076-I-I funded by MICIU/AEI/10.13039/501100011033 and by the European Union NextGenerationEU/PRTR. AFP thanks Comunidad de Madrid through the Talent Attraction Program (2020-T1/AMB-19799).

Conflict of Interests

The authors declare no conflict of interest.

Data Availability Statement

The datasets used during the current study are available in ZENODO repository (<https://zenodo.org/records/12703312>).

Keywords: Conjugated microporous polymer • Organic electrode material • Phenazine polymer • Polymer anode • Hydronium-ion battery • Organic manganese battery

- [1] J. M. Tarascon, M. Armand, *Nature* **2001**, *414* (6861), 359–367.
- [2] M. Li, J. Lu, Z. Chen, K. Amine, *Adv. Mater.* **2018**, *30*, 1800561.
- [3] L. Zhou, L. Liu, Z. Hao, Z. Yan, X. F. Yu, P. K. Chu, K. Zhang, J. Chen, *Matter* **2021**, *4*, 1252–1273.

- [4] J. Liu, C. Xu, Z. Chen, S. Ni, Z. X. Shen, *Green Energy & Environ.* **2018**, *3*, 20–41.
- [5] J. Li, H. Yan, C. Xu, Y. Liu, X. Zhang, M. Xia, L. Zhang, J. Shu, *Nano Energy* **2021**, *89*, 106400.
- [6] Z. Wu, P. Yang, S. Wang, S. Li, S. Zhang, *Trends Chem.* **2022**, *4*, 1121–1134.
- [7] Z. Tie, L. Liu, S. Deng, D. Zhao, Z. Niu, *Angew. Chem.* **2020**, *132*, 4950–4954.
- [8] N. Agmon, *Chem. Phys. Lett.* **1995**, *244*, 456–462.
- [9] Y. Xu, X. Wu, X. Ji, *Small Structures* **2021**, *2*, 2000113.
- [10] Y. H. Zhu, X. Yang, X. B. Zhang, *Angew. Chem. Int. Ed.* **2017**, *56*, 6378–6380.
- [11] W. Chen, G. Li, A. Pei, Y. Li, L. Liao, H. Wang, J. Wan, Z. Liang, G. Chen, H. Zhang, J. Wang, Y. Cui, *Nat. Energy* **2018**, *3*, 428–435.
- [12] G. Liang, F. Mo, H. Li, Z. Tang, Z. Liu, D. Wang, Q. Yang, L. Ma, C. Zhi, *Adv. Energy Mater.* **2019**, *9*, 1901838.
- [13] I. Aguilar, P. Lemaire, N. Ayouni, E. Bendadesse, A. V. Morozov, O. Sel, V. Balland, B. Limoges, A. M. Abakumov, E. Raymundo-Piñero, A. Slodczyk, A. Canizares, D. Larcher, J. M. Tarascon, *Energy Storage Mater.* **2022**, *53*, 238–253.
- [14] M. Wang, X. Zheng, X. Zhang, D. Chao, S. Z. Qiao, H. N. Alshareef, Y. Cui, W. Chen, *Adv. Energy Mater.* **2021**, *11*, 2002904.
- [15] Z. Zhang, W. Li, Y. Shen, R. Wang, H. Li, M. Zhou, W. Wang, K. Wang, K. Jiang, *J. Energy Storage* **2022**, *45*, 103729.
- [16] J. Huang, Z. Guo, X. Dong, D. Bin, Y. Wang, Y. Xia, *Sci. Bull.* **2019**, *64*, 1780–1787.
- [17] R. Liang, J. Fu, Y. P. Deng, Y. Pei, M. Zhang, A. Yu, Z. Chen, *Energy Storage Mater.* **2021**, *36*, 478–484.
- [18] L. Yan, J. Huang, Z. Guo, X. Dong, Z. Wang, Y. Wang, *ACS Energy Lett.* **2020**, *5*, 685–691.
- [19] Y. Wei, M. Zheng, W. Luo, B. Dai, J. Ren, M. Ma, T. Li, Y. Ma, *J. Energy Storage* **2022**, *45*, 103715.
- [20] J. J. Shea, C. Luo, *ACS Appl. Mater. Interfaces* **2020**, *12*, 5361–5380.
- [21] N. Goujon, N. Casado, N. Patil, R. Marcilla, D. Mecerreyes, *Prog. Polym. Sci.* **2021**, *122*, 101449.
- [22] X. Yang, Y. Ni, Y. Lu, Q. Zhang, J. Hou, G. Yang, X. Liu, W. Xie, Z. Yan, Q. Zhao, J. Chen, *Angew. Chem. Int. Ed.* **2022**, *61*, e202209642.
- [23] R. Emanuelsson, M. Sterby, M. Strømme, M. Sjödin, *J. Am. Chem. Soc.* **2017**, *139*, 4828–4834.
- [24] Y. Ma, Y. Wei, W. Han, Y. Tong, A. j. Song, J. Zhang, H. Li, X. Li, J. Yang, *Angew. Chem.* **2023**, *135*, e202314259.
- [25] C. Strietzel, M. Sterby, H. Huang, M. Strømme, R. Emanuelsson, M. Sjödin, *Angew. Chem. Int. Ed.* **2020**, *59*, 9631–9638.
- [26] N. Patil, A. Mavrandonakis, C. Jérôme, C. Detrembleur, J. Palma, R. Marcilla, *ACS Appl. Energ. Mater.* **2019**, *2*, 3035–3041.
- [27] W. Han, M. Li, Y. Ma, J. Yang, *Electrochim. Acta* **2022**, *403*, 139550.
- [28] Y. Li, Y. Lu, Y. Ni, S. Zheng, Z. Yan, K. Zhang, Q. Zhao, J. Chen, *J. Am. Chem. Soc.* **2022**, *144*, 8066–8072.
- [29] K. Oka, R. Löfgren, R. Emanuelsson, H. Nishide, K. Oyaizu, M. Strømme, M. Sjödin, *ChemElectroChem* **2020**, *7*, 3336–3340.
- [30] M. Yang, Q. Zhao, H. Ma, R. Li, Y. Wang, R. Zhou, J. Liu, X. Wang, Y. Hao, J. Ren, Z. Zheng, N. Zhang, M. Hu, J. Luo, J. Yang, *Small* **2023**, *19*, 2207487.
- [31] Y. Wang, C. Wang, W. Wang, Y. Zhang, Z. Guo, J. Huang, L. Yan, J. Ma, Y. Wang, *ACS Energy Lett.* **2023**, *8*, 1390–1396.
- [32] X. Wang, C. Bommier, Z. Jian, Z. Li, R. S. Chandrabose, I. A. Rodríguez-Pérez, P. A. Greaney, X. Ji, *Angew. Chem. Int. Ed.* **2017**, *56*, 2909–2913.
- [33] Y. Dai, X. Yan, J. Zhang, C. Wu, Q. Guo, J. Luo, M. Hu, J. Yang, *Electrochim. Acta* **2023**, *442*, 141870.
- [34] M. Shi, J. He, Y. Zhao, L. Zhao, K. Dai, C. Yan, *Mater. Des.* **2022**, *222*, 111043.
- [35] D. Alván, R. Grieco, N. Patil, A. Mavrandonakis, M. Liras, R. Marcilla, *Batteries & Supercaps* **2023**, *6*, e202300023.
- [36] J. He, Y. Zhao, C. Yan, R. Jing, R. Wang, M. Shi, *Chem. Eng. J.* **2023**, *470*, 144204.
- [37] A. Molina, N. Patil, E. Ventosa, M. Liras, J. Palma, R. Marcilla, *ACS Energy Lett.* **2020**, *5*, 2945–2953.
- [38] A. Molina, N. Patil, E. Ventosa, M. Liras, J. Palma, R. Marcilla, *Adv. Funct. Mater.* **2020**, *30*, 1908074.
- [39] R. Grieco, A. Molina, J. S. Sanchez, N. Patil, M. Liras, R. Marcilla, *Mater. Today Energy* **2022**, *27*, 101014.
- [40] J. S. Sanchez, Z. Xia, N. Patil, R. Grieco, J. Sun, U. Klement, R. Qiu, M. Christian, F. Liscio, V. Morandi, R. Marcilla, V. Palermo, *Small* **2022**, *18*, 2106403.
- [41] X. Wang, J. Zhou, W. Tang, *Energy Storage Mater.* **2021**, *36*, 1–9.
- [42] R. Grieco, O. Luzanin, D. Alvan, M. Liras, R. Dominko, N. Patil, J. Bitenc, R. Marcilla, *Faraday Discuss.* **2024**, *250*, 110–128.
- [43] T. Tomai, S. Mitani, D. Komatsu, Y. Kawaguchi, I. Honma, *Sci. Rep.* **2014**, *4*, 1–6.
- [44] X. Zhang, X. Zhang, Y. Miao, Q. Huang, Z. Chen, D. Guo, J. Xu, Y. M. Shen, J. Cao, *J. Mater. Chem. A* **2023**, *11*, 7152–7158.
- [45] X. Wu, J. J. Hong, W. Shin, L. Ma, T. Liu, X. Bi, Y. Yuan, Y. Qi, T. W. Surta, W. Huang, J. Neuefeind, T. Wu, P. A. Greaney, J. Lu, X. Ji, *Nat. Energy* **2019**, *4*, 123–130.
- [46] Z. Liu, L. Qin, B. Lu, X. Wu, S. Liang, J. Zhou, *ChemSusChem* **2022**, *15*, e202200348.
- [47] J. Huang, L. Yan, D. Bin, X. Dong, Y. Wang, Y. Xia, *J. Mater. Chem. A* **2020**, *8*, 5959–5967.
- [48] Z. Guo, J. Huang, X. Dong, Y. Xia, L. Yan, Z. Wang, Y. Wang, *Nat. Commun.* **2020**, *11*, 959.
- [49] T. Brezesinski, J. Wang, S. H. Tolbert, B. Dunn, *Nat. Mater.* **2010**, *9* (2), 146–151.
- [50] N. Patil, A. Mavrandonakis, C. Jérôme, C. Detrembleur, N. Casado, D. Mecerreyes, J. Palma, R. Marcilla, *J. Mater. Chem. A* **2021**, *9*, 505–514.
- [51] S. Perticari, T. Doizi, P. Soudan, C. Ewels, C. Latouche, D. Guyomard, F. Odobel, P. Poizot, J. Gaubicher, *Adv. Energy Mater.* **2019**, *9*, 1–16.
- [52] A. S. Pawar, M. T. Kolte, A. S. Pawar, M. T. Kolte, in *Plan. Hybrid Renew. Energy Syst. Electr. Veh. Microgrid*, Springer, Singapore, **2022**, pp. 553–583.
- [53] X. Dong, Z. Guo, Y. Wang, Y. Xia, *Joule* **2018**, *2*, 902–913.
- [54] J. Yu, J. Li, Z. Y. Leong, D. Sheng, Li, J. Lu, Q. Wang, H. Y. Yang, *Mater. Today Energy* **2021**, *22*, 100872.

Manuscript received: June 26, 2024

Accepted manuscript online: July 8, 2024

Version of record online: September 5, 2024